CPT: Pharmacometrics & Systems Pharmacology

ARTICLE OPEN ACCESS

Development and Verification of a Physiologically Based Pharmacokinetic Model of Furmonertinib and Its Main Metabolite for Drug–Drug Interaction Predictions

Yali Wu[1,2] | Helena Leonie Hanae Loer[3] | Yifan Zhang[1] | Dafang Zhong[1] | Yong Jiang[4] | Jie Hu[4] | Uwe Fuhr[2] | Thorsten Lehr[3] | Xingxing Diao[1]

[1]Shanghai Institute of Materia Medica, Chinese Academy of Sciences, Shanghai, China | [2]Clinical Pharmacology, Department I of Pharmacology, Center for Pharmacology, Faculty of Medicine and University Hospital Cologne, University of Cologne, Cologne, Germany | [3]Clinical Pharmacy, Saarland University, Saarbrücken, Germany | [4]Shanghai Allist Pharmaceuticals Co., Ltd, Shanghai, China

Correspondence: Uwe Fuhr (uwe.fuhr@uk-koeln.de) | Thorsten Lehr (thorsten.lehr@mx.uni-saarland.de) | Xingxing Diao (xxdiao@simm.ac.cn)

Received: 11 February 2025 | **Revised:** 30 April 2025 | **Accepted:** 13 May 2025

Funding: The authors Yali Wu obtained financial support provided by the China Scholarship Council during the study and manuscript preparation (No. 202204910415). The study was partially financially supported by the National Natural Science Foundation of China (Grant Nos. 82373938, 82204585), Key Technologies R&D Program of Guangdong Province (2023B1111030004), National Key R&D Program of China (2022YFF1202600).

ABSTRACT

Furmonertinib demonstrated potent efficacy as a newly developed tyrosine kinase inhibitor for the treatment of patients with epidermal growth factor receptor (EGFR) mutation-positive non-small cell lung cancer. In vitro research showed that furmonertinib is metabolized to its active metabolite AST5902 via the cytochrome P450 (CYP) enzyme CYP3A4. Furmonertinib is a strong CYP3A4 inducer, while the metabolite is a weaker CYP3A4 inducer. In clinical studies, nonlinear pharmacokinetics were observed during chronic dosing. The apparent clearance showed time- and dose-dependent increases. In this evaluation, a combination of in vitro data using radiolabeled compounds, clinical pharmacokinetic data, and drug–drug interaction (DDI) data of furmonertinib in oncology patients and/or in healthy subjects was used to develop a physiologically based pharmacokinetic (PBPK) model. The model was built in PK-Sim Version 11 using a total of 44 concentration-time profiles of furmonertinib and its metabolite AST5902. Suitability of the predictive model performance was demonstrated by both goodness-of-fit plots and statistical evaluation. The model predicted the observed monotherapy concentration profiles of furmonertinib well, with 32/32 predicted AUC_{last} (area under the curve until the last concentration measurement) values and 32/32 maximum plasma concentration (C_{max}) ratios being within twofold of the respective observed values. In addition, 8/8 predicted DDI AUC_{last} and C_{max} ratios with furmonertinib as a victim of CYP3A4 inhibition or induction were within twofold of their respective observed values. Potential applications of the final model include the prediction of DDIs for chronic administration of CYP3A4 perpetrators along with furmonertinib, considering auto-induction of furmonertinib and its metabolite AST5902.

1 | Introduction

The identification of targetable gene alterations has transformed the management of lung cancer by incorporating tumor genotyping to allow for individualized therapy. In the case of non-small cell lung cancer (NSCLC), mutations of the epidermal growth factor receptor (EGFR) can be cancer-driver genes, prompting the development of tyrosine kinase inhibitors (TKIs) against such oncogenic mutations [1, 2]. However, further mutations can develop providing drug resistance, among which a

Summary

- What is the current knowledge on the topic?
  - Based on preclinical and clinical studies, furmonertinib is metabolized via cytochrome P450 (CYP) 3A4, among others, to its active metabolite AST5902. Additionally, furmonertinib was identified as a strong inducer of CYP3A4 in vitro. Hence, CYP3A4 modulators can potentially alter furmonertinib's metabolism while furmonertinib itself can cause changes in the exposure of other CYP3A4 substrates. However, furmonertinib pharmacokinetic data is limited.
- What question did this study address?
  - This study addressed building a human physiologically based pharmacokinetic (PBPK) model of furmonertinib in PK-Sim with newly generated in vitro data using radiolabeled compound. The model is capable of evaluating the likely impact of chronic dosing of CYP3A34 modulators on furmonertinib and AST5902 exposure at steady state.
- What does this study add to our knowledge?
  - This study highlights the utility of PBPK modeling and simulation to assess the clinical drug–drug interaction (DDI) risk of furmonertinib. Our work established that furmonertinib is metabolized by multiple CYP isozymes, among which CYP2C9 and CYP3A4 are the most responsible for furmonertinib depletion, and CYP3A4 and CYP2C8 are most responsible for the metabolite formation. Overall, through modeling and simulation, the impact of chronic dosing of CYP3A4 perpetrators on exposure of furmonertinib at steady state was similar to clinical DDI study results when furmonertinib was only given as a single dose.
- How might this change drug discovery, development, and/or therapeutics?
  - This PBPK model can be utilized to simulate exposure in scenarios where clinical data may be lacking, including DDIs and special populations.

threonine-to-methionine substitution on codon 790 (T790M) is the most common case [3]. Furmonertinib is a selective EGFR TKI for treating patients with EGFR mutation-positive NSCLC. In 2021, furmonertinib was first approved in China for the treatment of patients with confirmed EGFR T790M mutation [4]. In both dose escalation and dose expansion studies, furmonertinib was well tolerated and no dose-limiting toxicity was found, demonstrating an acceptable toxicity profile with positive clinical efficacy [5].

Upon oral administration, furmonertinib is rapidly absorbed, with the time to maximum concentration (t_{max}) of total radioactivity reached after 0.5 h [6]. In vitro, furmonertinib was found to be mainly metabolized via cytochrome P450 (CYP) 3A4 to its main active metabolite AST5902. Moreover, furmonertinib showed an auto-induction effect on CYP3A4 similar to that of the strong inducer rifampicin (concentration for half-maximal induction (EC_{50}) 0.25 μM, maximum induction effect (E_{max}) as fold-induction up to 11.4), while for AST5902 only a much weaker induction ability was identified [7]. Regarding furmonertinib's pharmacokinetics (PK) in clinical trials, non-linear elimination was observed following multiple dose (MD) administration, displaying a time- and dose-dependent increase in apparent clearance, which is probably attributable to its auto-induction [7, 8].

Furthermore, furmonertinib's PK was demonstrated to differ between healthy subjects and patients. Following a single dose (SD) of 80 mg furmonertinib, healthy subjects exhibited a mean maximum plasma concentration (C_{max}) of 29.6 ng/mL and a mean area under the curve determined between time zero to time infinity ($AUC_{0-\infty}$) of 907 h*ng/mL, while for oncology patients mean C_{max} and $AUC_{0-\infty}$ values of 45.3 ng/mL and 1120 h*ng/mL, respectively, were observed [5, 9].

Furmonertinib is susceptible to drug–drug interactions (DDIs) when co-administered with CYP3A4 perpetrators. The $AUC_{0-\infty}$ of a SD administration of furmonertinib was increased by 141% when co-administered with the strong inhibitor itraconazole and decreased by 86% when co-administered with rifampicin as an inducer [9, 10]. Due to furmonertinib auto-induction of CYP3A4, the effect of perpetrators on the exposure of furmonertinib following MD administration might differ. Imatinib, for example, which also causes a clear change in CYP3A4 activity upon chronic administration (in this case, autoinhibition), has a decreased contribution of CYP3A4 to its metabolism during steady state compared to single dose administration [11]. However, DDI studies investigating the influence of CYP3A4 perpetrators on chronically administered furmonertinib are currently not available. To ensure safety and efficacy of furmonertinib therapy, its PK as well as the effect of CYP3A4 perpetrators on furmonertinib exposure following SD versus MD administration should be assessed in detail.

Here, physiologically based pharmacokinetic (PBPK) modeling provides a suitable framework as it allows the mechanistic description and prediction of furmonertinib's absorption, distribution, metabolism, and excretion (ADME) processes with and without co-medication. Moreover, the PBPK modeling approach enables a comprehensive investigation of the auto-induction effect of furmonertinib in terms of mechanism and impact on its PK. Physicochemical parameters as well as furmonertinib PK parameters obtained from in vitro experiments are important input parameters for PBPK model development but, in the case of furmonertinib, were only sparsely available prior to this work.

Thus, the aims of this study were (1) to provide data for a PBPK model by conducting in vitro experiments on ADME properties of furmonertinib and its metabolite AST5902; (2) to develop a human whole-body parent-metabolite PBPK model for furmonertinib and AST5902, incorporating parameters from the conducted in vitro experiments and in vivo pharmacokinetic profiles of SD and MD administrations in patients and healthy subjects; (3) to predict and investigate the effects of the CYP3A4 probe perpetrators itraconazole and rifampicin on SD versus MD furmonertinib administration. To promote widespread access and encourage further research, the finalized model files will be made available to the public at http://models.clinicalpharmacy.me/.

2 | Materials and Methods

2.1 | In Vitro Studies and Input Data

2.1.1 | Plasma and Microsomal Protein Binding Ratios With Radioactive Compounds

Fraction unbound (f_u) in human plasma was investigated with [^{14}C] labeled furmonertinib drug with rapid equilibrium dialysis (RED) equipment purchased from Thermo Scientific (Waltham, MA, USA). The hot stock solution was prepared in dimethyl sulfoxide (DMSO) at 10 mg/mL and then diluted into a 1 mg/mL working solution using methanol. Afterward, the working solution was diluted to 0.2 and 0.1 mg/mL using methanol:DMSO (9:1). Three different final concentrations of [^{14}C] furmonertinib in plasma were tested: 0.1, 0.2, and 1 μg/mL. The volume of the sample chamber was 200 μL plasma containing furmonertinib, and the buffer chamber was 400 μL phosphate-buffered saline (PBS). The plate was incubated at 37°C for 4 h with three replicates for each concentration. Then the samples from both chambers were pipetted to Deepwell LumaPlate 96-well plates (Perkin Elmer, MA, USA) and the radioactive concentrations of both sides were measured with a Hidex Sense Beta microplate reader (Hidex, Turku, Finland). The f_u in human microsomes was measured in a similar way: The incubation concentration of human microsomes was 0.1 mg/mL, and the drug concentrations were the same as in plasma. The f_u in both matrices was calculated as follows: % free = (concentration in buffer chamber/concentration in matrices chamber) × 100%.

2.1.2 | Caco-2 Permeability- Calculating P_{app} Value

The absorption of orally administrated furmonertinib was predicted with permeability coefficients across monolayers of the human colon carcinoma cell line Caco-2 [12]. Caco-2 cells were transferred to each well of 24-well transport plates and incubated at 37°C/5% CO_2 for 21 days. Final concentrations of 15 and 45 μM of furmonertinib were tested on the donor and receiver sides, respectively. Samples were withdrawn from the donor side at 5 min for recovery calculations. After 95 min, samples from both basolateral sides and apical sides of the filter were withdrawn. The radioactive concentrations on each side were measured with a liquid scintillation counter (Tri-Carb 3110TR, PerkinElmer, Waltham, MA, USA). The apparent permeability coefficient (P_{app}) was calculated as follows: $P_{app} = (V_R/(\text{Area} \times \text{Time})) \times ([\text{drug}]_{\text{receiver}}$ at 95 min/$[\text{drug}]_{\text{donor}}$ at 5 min), where V_R is the volume in the receiver wells, area is the surface area of the membrane, and time is the total transport time in seconds.

2.1.3 | Phenotyping Furmonertinib and AST5902 Depletion/Formation Using Recombinant P450 Enzyme Studies

All incubations were prepared in a 37°C water bath in triplicates. Eight recombinant CYP enzymes were assessed, and reaction rates were measured. The depletion of 1 μM furmonertinib and AST5902 by CYP1A2, CYP2B6, CYP2C8, CYP2C9, CYP2C19, CYP2D6, CYP3A4, and CYP3A5 was investigated with the addition of 1 mM β-NADPH to initiate the reaction in a 75-min incubation. All enzymes in the incubations had the same final concentrations of 25 pmol/mL. The samples were collected at different time points, and the reactions were terminated with acetonitrile containing an internal standard (furmonertinib-d3). Subsequently, the mixture was shaken for 10 min to allow precipitation before being centrifuged. The concentrations of furmonertinib and AST5902 were quantified with the LC–MS/MS method as previously described [13]. Standard curves were prepared separately with each experiment for absolute quantification.

2.1.4 | Michaelis–Menten Kinetic Profiling Using Human Liver Microsomes

The enzyme kinetics of AST5902 formation was determined by incubating furmonertinib with different initial concentrations. The linearity of the reaction was first tested with three different concentrations (final concentrations of 0.1, 0.2, and 0.5 mg/mL) of human liver microsomes (HLMs, purchased from Corning, Corning, NY, USA). Samples were collected at 0, 5, 15, 30, 45, and 60 min. A concentration of 0.1 mg/mL HLM was used for subsequent Michaelis–Menten kinetic experiments. Formation kinetic parameters (the Michaelis constant K_M and maximal formation rate V_{max}) of AST5902 were obtained by fitting the Michaelis–Menten kinetic Equation (1) to the AST5902 formation rate (V) versus furmonertinib concentration ($[S]$). The formation clearance of AST5902 in HLM was calculated according to Equation (2). All other procedures were as described for incubations with recombinant enzymes.

$$V = \frac{V_{max} \bullet [S]}{K_M + [S]} \quad (1)$$

$$CL_{HLM} = \frac{V_{max}}{K_M} \quad (2)$$

The Michaelis–Menten kinetic experiments were repeated on three independent occasions.

2.1.5 | Software

PK-Sim Version 11 (Open Systems Pharmacology Suite, www.open-systems-pharmacology.org, 2022) was used for the development of the furmonertinib and AST5902 parent-metabolite PBPK model, the evaluation of the model, and sensitivity analyses. The compilation of plots as well as calculations of PK parameters and quantitative model performance measures were performed using the R programming language version 4.2.3 (R Foundation for Statistical Computing, https://www.r-project.org).

2.2 | Clinical Study Data

Published clinical study data were obtained from Shanghai Allist Pharmaceuticals Co. Ltd. The clinical study in patients covered a broad dosing range of furmonertinib from 20 to 240 mg administered orally, including SD and MD

administrations. The DDI models, which investigated furmonertinib as a CYP3A4 victim drug, were developed with two different studies in healthy subjects [9, 10]. In these studies, itraconazole was co-administered as a CYP3A4 competitive inhibitor and rifampicin as a strong CYP3A4 inducer and a weaker inducer of CYP2C8. Subjects in both studies were pretreated with either itraconazole (13 days, 0.2 g, twice daily) or rifampicin (16 days, 0.6 g, once daily) followed by an SD administration of 80 mg furmonertinib. All profiles were divided into a training dataset for model development and a test dataset for model evaluation. The training dataset was assembled to: (1) include DDI studies for better identification and information on metabolic pathways and (2) cover SD and MD administrations over a wide range of dosages to provide dense information on CYP3A4 auto-induction. All details, including dose and demographic information on the clinical studies used, are described in Table S2.

2.3 | PBPK Model Building

The PBPK model for furmonertinib and its metabolite was developed using a stepwise modification approach. For each study population, a representative East Asian virtual individual was built based on the reported mean data for age, weight, height, and body mass index. Relative expression of relevant transporters and enzymes in different organs was implemented according to the PK-Sim expression database as described in Table S1.

Model development was initiated using the information on the ADME processes of furmonertinib and its metabolite from in vitro experiments. The induction parameters (EC_{50} and E_{max}) of furmonertinib and AST5902 had already been published [7]. The majority of parameters, including f_u in plasma and microsomes, P_{app} values, fraction metabolized via different enzymes, and kinetic parameters generated from microsomes, were obtained in this study, as mentioned before. First, data from SD administration in healthy subjects was used to determine the calculation methods for cellular permeability and partition coefficients. The dissolution was described using a Weibull function as described in Section S1.4. Both 50% dissolution time and dissolution shape were estimated. Then, the DDI studies with rifampicin and itraconazole as perpetrators in healthy subjects were used to refine the metabolic pathways and fractional contributions of different CYP enzymes. We started with the simple pathway—CYP3A4 only—and added further enzymes one by one until there was no significant improvement in the model. After validating the model in healthy subjects, patient data was used to perform patient-specific model adjustments regarding absorption, metabolism, and auto-induction parameters using SD and MD administrations of furmonertinib. The model development diagram is shown in Figure 1. As CYP2C8 and CYP3A4 were identified as the two enzymes predominantly responsible for the formation of the active metabolite, they were implemented in the model. For the drug depletion metabolism, CYP3A4, CYP2C8, CYP2C9, and CYP1A2 were incorporated into the model according to the in vitro f_m values. Other enzymes with negligible contributions, for example, CYP2D6 (< 1%), were not included in the model.

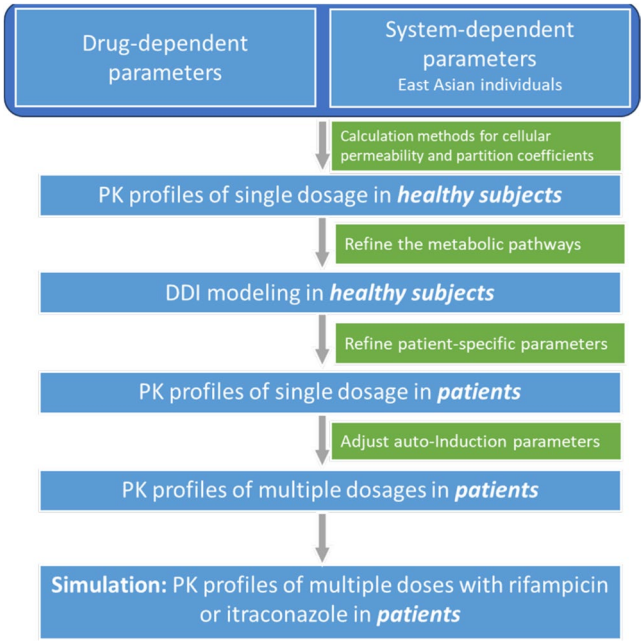

FIGURE 1 | Stepwise model development diagram.

2.4 | PBPK Model Evaluation

A series of goodness-of-fit (GOF) plots were created for the comparison of concentrations between predicted and observed profiles. Moreover, GOF plots were used to compare predicted key PK parameters, that is, AUC determined between first and last concentration measurements (AUC_{last}) and C_{max}, to observed values.

Statistical evaluation was conducted to investigate the deviation of predicted to observed concentrations. Mean relative deviations (MRDs) (Equation 3) for all predicted plasma concentrations and geometric mean fold errors (GMFEs) (Equation 4) for all predicted AUC_{last} and C_{max} values were calculated.

$$\mathrm{MRD} = 10^{x}; x = \sqrt{\frac{\sum_{i=1}^{k} \left(\log_{10}\hat{c}_i - \log_{10}c_i\right)^2}{k}} \tag{3}$$

where c_i = ith observed concentration, $\hat{c}_i$ = the corresponding ith predicted concentration, and k = number of observed values.

$$\mathrm{GMFE} = 10^{x}; x = \frac{\sum_{i}^{m} \left|\log_{10}\left(\frac{\hat{\rho}_i}{\rho_i}\right)\right|}{m} \tag{4}$$

where ρ_i = observed AUC_{last} or C_{max} value of study i, $\hat{\rho}_i$ = the corresponding predicted AUC_{last} or C_{max} value of study i, and m = number of studies.

Model-based population simulations were created for visual check with the observed plasma concentration profiles. For this, virtual populations were created based on the characteristics from each clinical trial cohort. For each study, 1000 individuals were created with variability in enzyme expression and demographics. Geometric standard deviations of the implemented enzyme and transporter concentrations are shown in Table S1.

Local sensitivity analyses were performed as described in Section S3.4.1. Parameters evaluated during local sensitivity analyses were listed in Tables S11 and S12.

2.5 | DDI Modeling

DDI studies investigating the influence of the CYP3A4 perpetrators itraconazole and rifampicin on furmonertinib exposure were used for DDI modeling. The previously published PBPK model files of itraconazole and rifampicin [14] were downloaded from https://github.com/Open-Systems-Pharmacology/Itraconazole-Model/tree/v1.3 and https://github.com/Open-Systems-Pharmacology/Rifampicin-Model/tree/v1.2. All the relevant interaction parameters were incorporated from the literature as described in Tables S14 and S15.

The DDI models were evaluated analogously to the base PBPK model. Additionally, the models were assessed by comparing the DDI PK parameter ratios applying the limits proposed by Guest et al. to determine prediction accuracy allowing 20% variability [15] (Equation 5):

$$\text{DDI PK parameter ratio} = \frac{\text{PK parameter}_{\text{without perpetrator}}}{\text{PK parameter}_{\text{with perpetrator}}} \quad (5)$$

where PK parameter $= \text{AUC}_{\text{last}}$ or $C_{\max}$, PK parameter$_{\text{without perpetrator}} = \text{AUC}_{\text{last}}$ or $C_{\max}$ of furmonertinib or metabolite in control group while PK parameter$_{\text{with perpetrator}} = \text{AUC}_{\text{last}}$ or $C_{\max}$ of furmonertinib or metabolite co-administered with itraconazole or rifampicin.

2.6 | Model Application

The established PBPK model was used for prospective predictions when furmonertinib would be concomitantly administrated with CYP3A4 perpetrators in the long term. Itraconazole was used as a strong CYP3A4 inhibitor, and rifampicin was used as a strong CYP3A4 inducer. The virtual individuals were created based on the mean profile of the clinical DDI study population for comparisons. The parent drug, active metabolite, and the sum of both, that is, the total active components, were simulated. The model was used for the prediction of the following two different scenarios: (1) pharmacokinetic profiles of oncology patients who received 21 days of 80 mg furmonertinib to reach steady state, followed by co-administration with itraconazole (200 mg, twice daily) for 7 days; (2) pharmacokinetic profiles of oncology patients who received 21 days of 80 mg furmonertinib to reach steady state, followed by co-administration with rifampicin (600 mg, once daily) for 7 days.

3 | Results

3.1 | In Vitro Assays

The plasma protein assays identified a f_u value of 0.63% for furmonertinib (Table S4). As for the protein assays in microsomes, an incomplete recovery of radioactivity was observed, and it suggested a value of f_u in microsomes from 3.17% to 39.8% for further optimization. In the Caco-2 drug permeability assays, an incomplete recovery of radioactivity was also observed when only measuring the radioactivity in the basolateral side and apical side. After digesting the cells from the cell culture plate and measuring the radioactivity of lysates, the recovery was 88.4% (Table S5).

Using eight different recombinant CYP enzymes, CYP3A4, CYP2C8, CYP2C9, and CYP1A2 were found to be the most relevant enzymes regarding the depletion of furmonertinib and AST5902. Additionally, CYP3A4, CYP2C8, and CYP3A5 were found to be relevant regarding the formation of AST5902. CYP3A4 was the major enzyme responsible for the depletion of furmonertinib and AST5902 as well as the formation of AST5902 with fraction metabolized (f_m) values of 80.2%, 53.0%, and 83.3%, respectively. The details of all first-order kinetic parameters are described in Section S2.3.

The metabolite formation approach was used to estimate the formation kinetics of AST5902 in pooled HLMs. The $V_{\max}$ and K_{M} values were (mean ± standard deviation) 0.89 ± 0.12 nmol/min/mg protein and 3.72 ± 1.75 μM, respectively. The calculated metabolite formation clearance (mean ± standard deviation) of AST5902 was 0.28 ± 0.13 mL/min/mg protein. The calculation methods are described in detail in Sections S2.3 and S2.4.

3.2 | PBPK Model Building and Evaluation

The data profiles were obtained from six clinical trials and separated into training and test datasets. There were two populations, that is, healthy subjects and patients, involved, as described in Table S2.

The metabolism of furmonertinib was implemented via CYP3A4, CYP2C8, CYP2C9, and CYP1A2, with initial intrinsic clearances adopted from the conducted phenotyping experiments. Here, CYP2C8 and CYP3A4 lead to the formation of the metabolite, while CYP1A2, CYP2C9, and part of the metabolism via CYP3A4 resulted in undefined metabolites. CYP1A2, CYP2C9, and CYP3A4 were implemented for the disposition of AST5902. Figure 2 presents a schematic overview of the modeled metabolic pathways.

The patient-specific parameters were refined using SD profiles from patients. The CYP3A4 clearance for the sink pathway was fitted to 0.60 L/μmol/min in healthy subjects and was further optimized to 0.29 L/μmol/min in patients. The specific intestinal permeability in patients was optimized as 7.24×10^{-5} cm/min compared to the in vitro values used in healthy subjects, which are 3.18×10^{-5} cm/min. The EC_{50} and $E_{\max}$ values of furmonertinib were further fitted as 0.49 μM and 12.25 using MD studies in patients compared to the experimental values, which are 0.25 μM and 9.28.

In vitro, the f_m of CYP3A4 and CYP2C8 responsible for metabolite formation were calculated as 83.3% and 16.5%. In patient model simulation, the values were 94.5% and 5.5%, respectively. As for the parent drug depletion, f_m of CYP3A4 and CYP2C9 were 80.2% and 5.56% in experiments, while in the PBPK model,

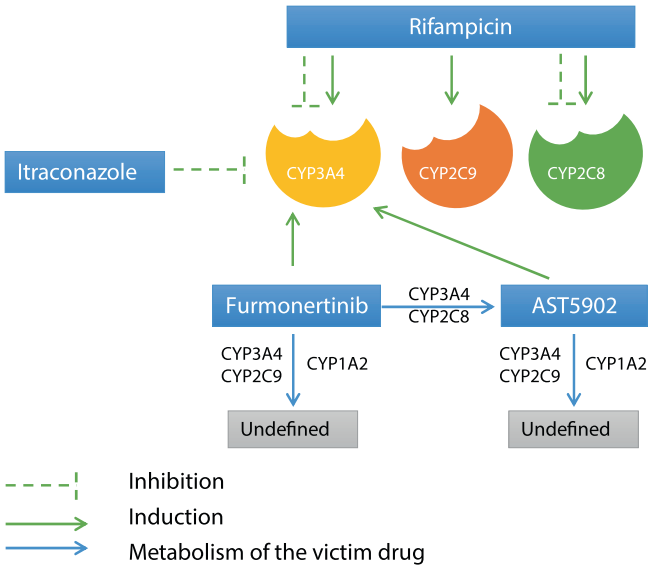

FIGURE 2 | Overview of the metabolic pathways involved in the furmonertinib PBPK model and the modeled drug–drug interactions. CYP, cytochrome P450; PBPK, physiologically based pharmacokinetic.

CYP3A4 contributed 48.7% (10.4% to form the metabolite and 38.4% in the sink pathway) and CYP2C9 contributed 49.9% in healthy subjects.

A detailed review of all furmonertinib and AST5902 model parameters is summarized in Table 1. A table of all key modeling assumptions as well as the model decisions can be found in Table S3.

Overall, the developed PBPK model of furmonertinib and AST5902 showed good descriptive (training dataset) and predictive (test dataset) performance. For the test and training datasets, exemplary plasma concentration-time profiles following 80 mg administration to patients are provided in Figure 3. Semilogarithmic and linear plots of all predicted and observed profiles are provided in Sections S3.1 and S3.2.

Figure 4 displays GOF plots of predicted versus observed concentration measurements, AUC_{last} and C_{max} values stratified by training and test datasets, separated by patients and healthy subjects. In healthy subjects, 92.4% of all predicted concentration measurements were simulated within twofold of their corresponding observed data. 12/12 of predicted AUC_{last} and C_{max} values were simulated within twofold of their values calculated from the observed concentration-time profile. The calculated mean MRD value is 1.61, mean $GFME_{AUClast}$ is 1.28, and mean $GMFE_{Cmax}$ value is 1.30, including training and test datasets. In patients, 93.3% of all predicted concentration measurements were simulated within twofold of their corresponding observed data. 32/32 of predicted AUC_{last} and C_{max} values were simulated within twofold of their values calculated from the observed concentration-time profile. The good descriptive and predictive performance of the model in patients could be further demonstrated by the calculated mean MRD values. For the training dataset, the mean MRD value is 1.56, while for the test dataset, the value is 1.37. For every profile used, MRD and GMFE values are listed in Tables S9 and S10.

Local sensitivity analyses were performed for furmonertinib and AST5902 with respect to healthy subjects and patients. The AUC_{last} of furmonertinib in both patients and healthy subjects was determined to be most sensitive to changes in furmonertinib acid dissociation constant, while for AST5902, the AUC_{last} was determined to be most sensitive to changes in furmonertinib lipophilicity. A detailed assessment of the sensitivity analyses can be found in Section S3.4.

3.3 | DDI Modeling

The modeled DDI network is presented in Figure 2. Other details, including the model file of itraconazole and rifampicin as well as model parameters of the DDI models, are provided in Section S4.

Figure 5 shows the predicted versus observed plasma concentration-time profiles of furmonertinib administered alone or concomitantly with itraconazole or rifampicin. Figure 5a–d demonstrates the plasma concentration-time profiles of population simulations of the DDI studies. For each study, predicted versus observed AUC_{last} and C_{max} values are displayed in Figure 5e,f, with the limits proposed by Guest et al. [15]. All linear and semilogarithmic plots of predicted versus observed plasma concentration-time profiles are available in Sections S4.3 and S4.4.

In a clinical DDI study, the impact of rifampicin on the exposure of a single-dose (SD) administration of furmonertinib was evaluated. Chronic rifampicin dosing resulted in an 86.7% decrease in furmonertinib AUC_{0-t} and a 60.3% decrease in total active ingredient exposure (AUC_{0-t}), which closely matched PBPK model predictions of 70.8% and 47.4% reduction, respectively.

In a clinical DDI study, when co-administered with itraconazole, the AUC_{0-t} of furmonertinib and total active ingredients increased by 120.8% and 48.1%, which closely matched PBPK model predictions of 130.3% and 41.1%, respectively.

3.4 | Model Application

The simulations are displayed in Figure 6. Subsequent model simulations in patients on the effects of chronic rifampicin dosing on the steady-state AUC of furmonertinib suggested a reduced effect compared to SD administration of furmonertinib, as the exposure of furmonertinib and total active ingredients was only decreased by 48.6% and 37.6%, respectively. Subsequent model simulations in patients on the effects of chronic itraconazole dosing on the steady-state AUC of furmonertinib suggested a similar effect compared to SD administration of furmonertinib, as the exposure of furmonertinib and total active ingredients increased by 141.0% and 47.1%, respectively.

4 | Discussion

In this present work, a whole-body PBPK model for furmonertinib and its active metabolite AST5902 was built and evaluated, in part based on novel in vitro data. The metabolite AST5902 is an active metabolite with drug efficacy similar to that of the

TABLE 1 | Drug-dependent parameters of the final furmonertinib parent-metabolite PBPK model.

		Furmonertinib				Metabolite			
		Healthy		Patients		Healthy		Patients	
Parameter	**Unit**	**Value**	**Source**	**Value**	**Source**	**Value**	**Source**	**Value**	**Source**
Molecular weight	g/mol	568.61	Lit. (13)	568.61	Lit. (13)	554.58	Lit. (13)	554.58	Lit. (13)
pKa, base	—	8.69	In vitro	8.69	In vitro	9.34	In silico	9.34	In silico
Solubility (pH)	mg/mL	3.36 (5[c])	In vitro	3.36 (5[c])	In vitro	0.48 (10.01)	In silico	0.48 (10.01)	In silico
Lipophilicity	Log units	4.03	(2.94[c]) Opt.	4.03	(2.94[c]) Opt.	4.30	Opt.	4.30	Opt.
f_u[a]	%	0.63	In vitro	0.63	In vitro	7.48	In silico	7.48	In silico
GFR fraction	—	1.00	Asm.	1.00	Asm.	1.00	Asm.	1.00	Asm.
Specific intestinal permeability[a,b]	cm/min	3.18×10^{-5}	In vitro	7.24×10^{-5}	Opt. (in vitro)	1.16×10^{-5}	In silico	1.16×10^{-5}	In silico
Dissolution time (Weibull, 50% dissolved)	min	20.53	Opt.	20.53	Opt.	—	—	—	—
Dissolution shape (Weibull)	—	1.03	Opt.	1.03	Opt.	—	—	—	—
CYP2C8 Clearance—metabolite[b]	L/μmol/min	0.22 (0.50)	Opt. (in vitro)	0.22 (0.50)	Opt. (in vitro)	—	—	—	—
CYP3A4 k_{cat}—metabolite[b]	1/min	0.82 (8.20)	Opt. (in vitro)	0.82 (8.20)	Opt. (in vitro)	—	—	—	—
CYP3A4 K_M	μmol/L		3.72 (in vitro)		3.72 (in vitro)				
CYP2C9 Clearance—Sink[a]	L/μmol/min	1.21 (0.30)	Opt. (in vitro)	1.21 (0.30)	Opt. (in vitro)	0.12 (0.30)	Opt. (in vitro)	0.12 (0.30)	Opt. (in vitro)
CYP1A2 Clearance—Sink[a]	L/μmol/min	0.08 (0.45)	Opt. (in vitro)	0.08 (0.45)	Opt. (in vitro)	1.05 (0.56)	Opt. (in vitro)	1.05 (0.56)	Opt. (in vitro)
CYP3A4 Clearance—Sink[a,b]	L/μmol/min	0.60 (1.00)	Opt. (in vitro)	0.29 (1.00)	Opt. (in vitro)	7.07×10^{-3} (1.00)	Opt. (in vitro)	7.07×10^{-3} (1.00)	Opt. (in vitro)
CYP3A4 E_{max}[b]	—	9.28	Lit. (7)	12.25 (9.28)	Opt. (in vitro)	2.00	Lit. (7)	2.64 (2.00)	Opt. (in vitro)
CYP3A4 EC_{50}[b]	μmol/L	0.25	Lit. (7)	0.49 (0.25)	Opt. (in vitro)	0.33	Lit. (7)	0.65 (0.33)	Opt. (in vitro)

Note: In silico: Parameters were predicted with ADMET predictor.
Abbreviations: Asm., assumed; CYP, cytochrome P450; EC_{50}, half maximum effect concentration; E_{max}, maximum effect; f_u, fraction unbound; k_{cat}, catalytic rate constant; K_M, Michaelis–Menten constant; lit., literature; Opt., optimized; PBPK, physiologically based pharmacokinetic; pKa, acid dissociation constant.
[a]In vitro parameters were obtained from experiments in this study.
[b]Parameter optimized for patient population.
[c]Parameter provided by Shanghai Allist Pharmaceuticals Co. Ltd.

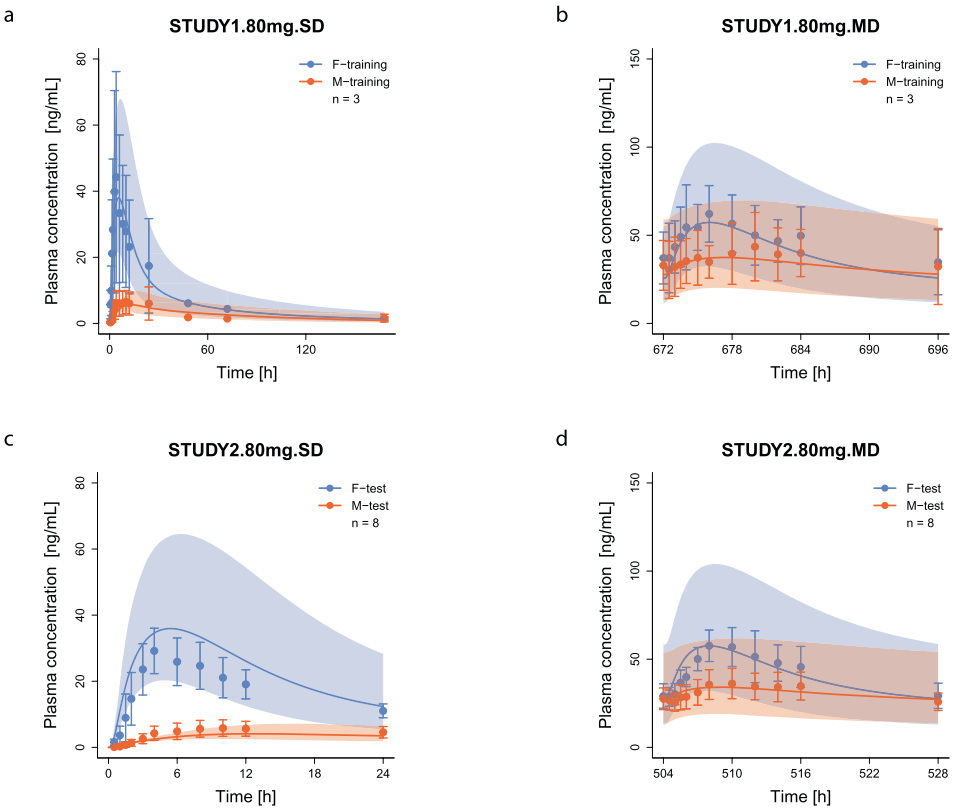

FIGURE 3 | Exemplary plots of plasma concentration profiles of furmonertinib and the metabolite AST5902 following 80 mg furmonertinib multiple-dose administration in patients. Stratified by training (a, b) and test (c, d) datasets, including single dose (a, c) and steady state (b, d) profiles; *F* represents furmonertinib and *M* represents the metabolite AST5902; solid lines and ribbons represent population predictions ($n = 1000$; geometric mean and geometric standard deviation), whereas corresponding observations are shown as dots (±standard deviation). Detailed information on all investigated profiles is provided in Sections S3.1 and S3.2.

parent compound, making it clinically relevant. During chronic administration, the exposure levels of the metabolite are comparable to those of furmonertinib, so including its PK profile aids in understanding the overall metabolic pathways of furmonertinib. The PK of furmonertinib and its metabolite were successfully described and predicted for a broad dosing range (20–240 mg) of orally administrated furmonertinib with and without co-administration of CYP3A4 perpetrators in healthy volunteers and in patients.

The special characteristics of protein binding exert difficulties in the in vitro/in vivo extrapolation. For TKIs, some of them exert effects on the target protein via covalent binding, for example, osimertinib and furmonertinib. However, it has been found in recent years that these compounds could bind with other proteins as well, resulting in a low recovery in matrix, for example, plasma [6, 16–18]. In the development of osimertinib PBPK modeling, researchers also found that this binding character could result in the inaccuracy of in vitro/in vivo extrapolation, especially when translating the permeability parameters like P_{app} value from Caco-2 monolayer assay and calculating the f_u in plasma and microsomes [19]. The use of radiolabeled [^{14}C] furmonertinib ensured comprehensive detection of both parent drug and any covalently bound or trapped forms, minimizing underestimation of total drug movement. In our study, specific intestinal permeability was also adjusted during model optimization to reconcile in vitro recovery limitations with observed clinical absorption rates (e.g., faster absorption in patients required increasing intestinal permeability). It is worth mentioning that a low recovery was found when calculating the f_u values of furmonertinib in microsomes. This could be attributed to unspecific binding with the device. Thus, a range of f_u in microsomes was calculated, supposing all the binding part belongs to the buffer side or the matrices side. However, considering that f_u value obtained is not reliable, we used the original value of K_M (3.72 μM) in the model.

The gut microbiota affects drug PK and anticancer activity at various levels [20, 21]. Cancer cell presence may trigger alterations of gut barrier function, which is often accompanied by translocation of microbial antigens in other organs such as the liver [22, 23]. In the model, different intestinal permeability values were optimized for patients and healthy subjects to capture the overall higher C_{max} observed in patients than in healthy subjects (45.3 ng/mL vs. 29.6 ng/mL). The specific intestinal permeability of furmonertinib in healthy subjects was 3.18×10^{-5} cm/min (generated from Caco-2 drug permeability assays), while for patients a value of 7.24×10^{-5} cm/min was optimized. The metabolism of the parent drug was also investigated, respectively, in patients and healthy subjects, considering that published reports claimed that cancer patients could have lower capability for drug metabolism than healthy people [24–28]. During model building, a patient-specific adjustment of the different k_{cat} values used for metabolite formation and the CYP3A4 clearance of the sink pathway were tested. Here, a decrease in CYP3A4 sink pathway clearance

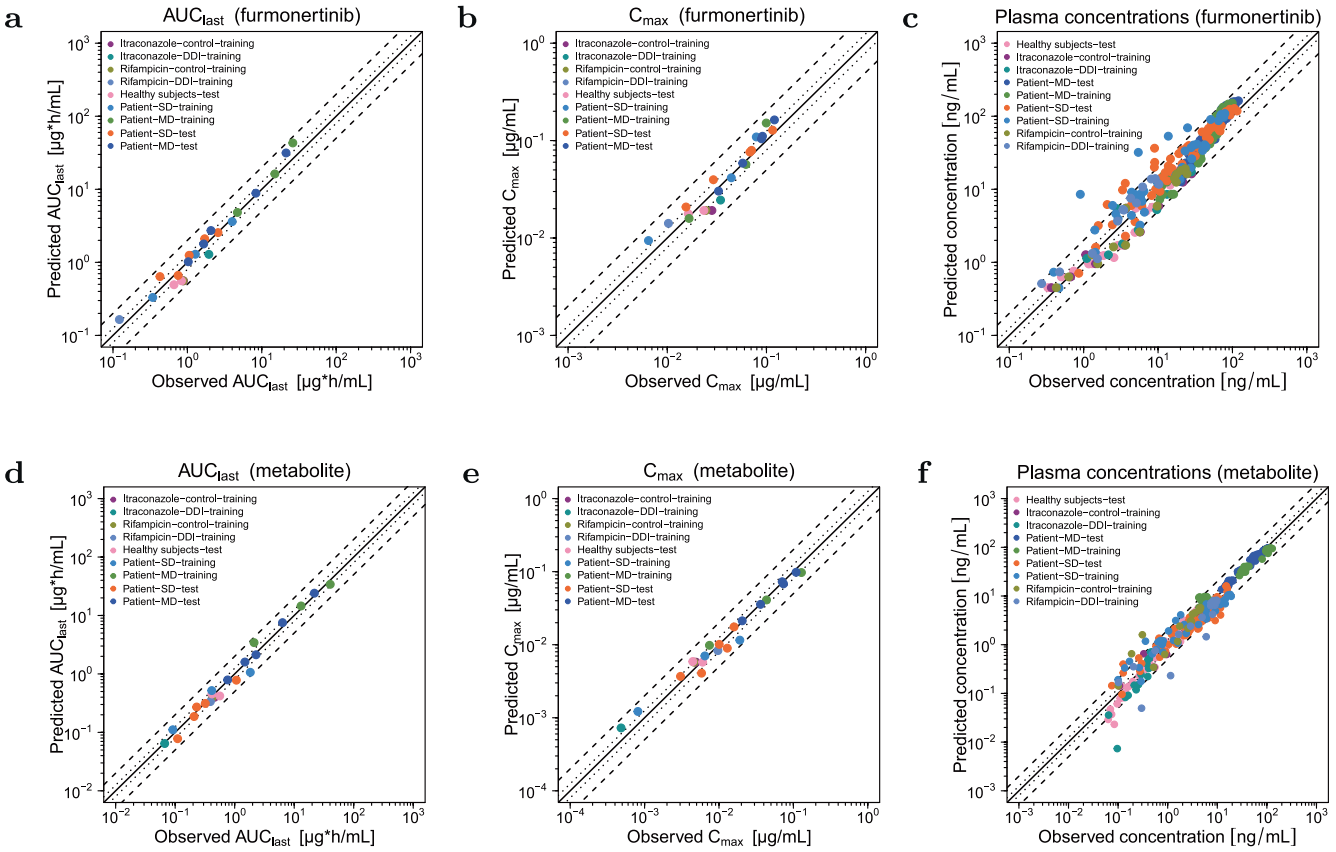

FIGURE 4 | Goodness-of-fit plots of the final furmonertinib model for healthy individuals and patients. Stratified by parent drug (upper row) and metabolite (lower row), predicted plasma concentration measurements as well as AUClast, C_{max} are plotted against corresponding observed data. The solid line represents the line of identity, whereas dotted lines indicate 1.25-fold, and dashed lines indicate twofold deviation from the respective observed value. AUClast, area under the curve determined between first and last concentration measurements; C_{max}, maximum plasma concentration.

greatly improved the prediction performance of the patients' profiles (0.6 L/µmol/min in healthy subjects and 0.29 L/µmol/min in patients). The auto-induction parameters E_{max} and EC_{50} were only adjusted upon inclusion of MD applications to patients in the parameter optimization process, as during the initial optimization steps with healthy subjects only SD administrations were available, in which auto-induction does not play a pronounced role. To verify, we later tested the E_{max} and EC_{50} values optimized from MD patient data on SD healthy profiles and found no impact on predictions for healthy subjects in SD scenarios. However, we could not verify MD predictions in healthy subjects, as no MD data are available for this population.

Furmonertinib metabolism involves a complex interplay of CYP enzymes; the depletion and formation clearance mediated by CYP isozymes were optimized with clinical DDI studies involving CYP3A4 perpetrators. However, in vivo PBPK simulations revealed shifts in relative enzymatic contributions compared to in vitro observation, particularly an amplified role for CYP3A4 in metabolite formation and a marked increase in CYP2C9-mediated parent depletion. This discrepancy could arise from differing affinities of CYP2C9 and CYP3A4 to furmonertinib. Since the Michaelis–Menten kinetics of furmonertinib were obtained in HLMs, we could not isolate the specific affinity parameters for CYP2C9 and CYP3A4 in our model.

There are also some limitations to this PBPK model. All the clinical studies involved in this research were conducted in Chinese people. In the model development, all individuals and populations were created based on the East Asian population embedded in PK-Sim. In the future, more clinical studies should be included to investigate the effect of ethnicity on the PK of furmonertinib and AST5902. Moreover, CYP2C9 is highly polymorphic and plays an important role in the metabolism of furmonertinib, with apparent major differences between in vitro studies and *the vivo* situation as described in the PBPK model. However, as no CYP2C9 genotyping had been performed for the included study populations and no DDI studies with selective CYP2C9 perpetrators were conducted, different CYP2C9 activity levels could not be considered in this study. Moreover, although we already optimized E_{max} to a relatively high value (12.3 in the model compared to 9.28 in vitro), the concentrations of furmonertinib predicted in higher dosage groups (e.g., 160 mg and 240 mg) are still over-predicted, and the concentrations of the metabolite are under-predicted, suggesting an even higher E_{max} value of CYP3A4. In the depletion of furmonertinib, CYP2C9 also plays an important role, and both CYP2C9 and CYP3A4 can be induced through the pregnane X Receptor (PXR) pathway [29–34]. However, in vitro induction studies on furmonertinib showed no significant induction of CYP2C9. These findings were previously published in tab. 4 of a related article [8]. The absence of furmonertinib CYP2C9 induction in our model did not compromise the accuracy of our diagnostics,

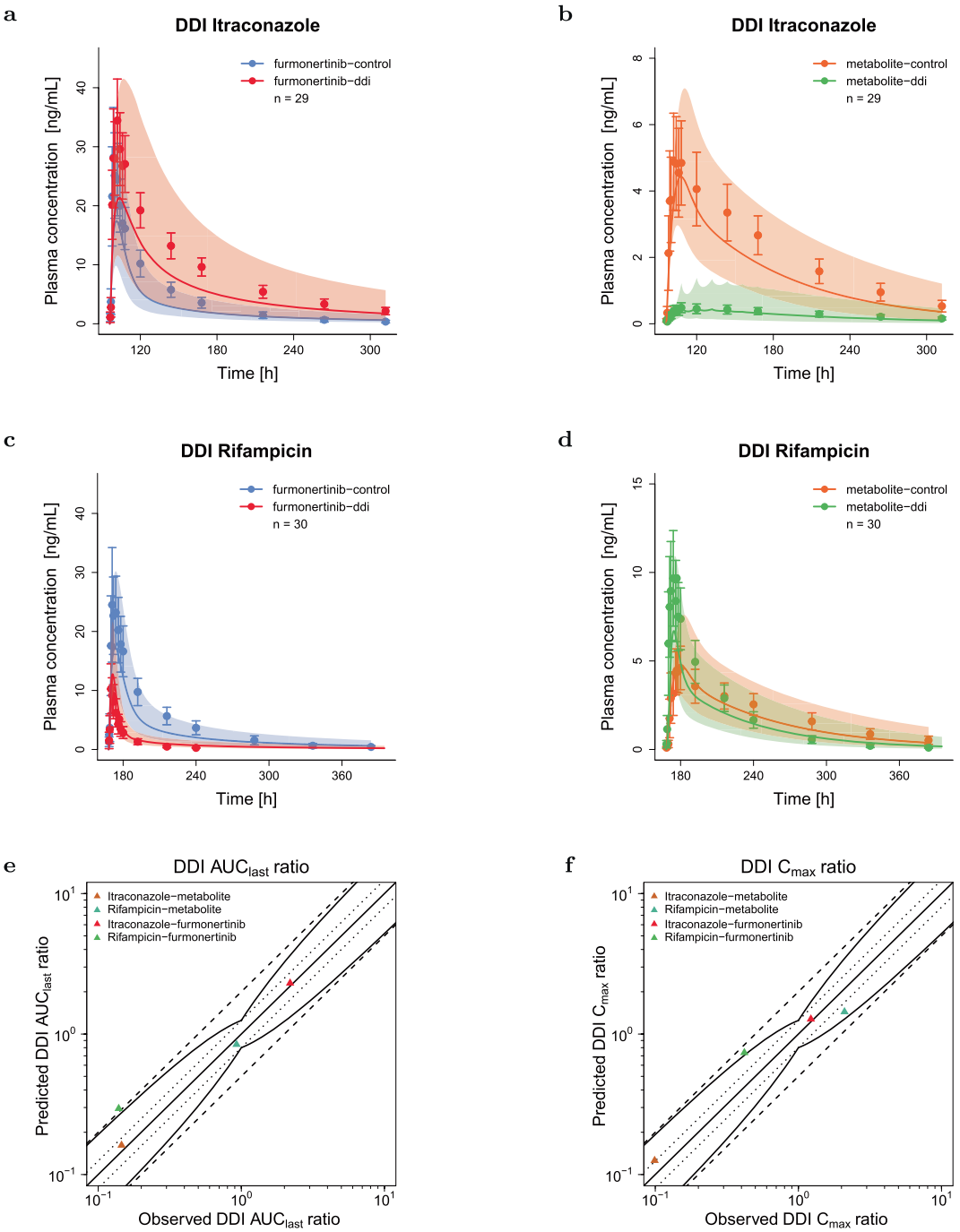

FIGURE 5 | Evaluation of the modeled DDI simulations. (a, b) represent the itraconazole-furmonertinib-DDI study and (c, d) represent the rifampicin-furmonertinib-DDI study. The predicted plasma concentration-time profiles of furmonertinib or metabolite are presented alongside their observed data. Solid lines and ribbons represent population predictions ($n = 1000$; geometric mean and geometric standard deviation), whereas corresponding observations are shown as dots (±standard deviation). Predicted versus observed DDI AUClast (e) and DDI C_{max} (f) ratios are shown, with the solid line representing the line of identity, dotted lines indicating 1.25-fold and dashed lines indicating two-fold deviation from the respective observed value, along with the curved lines marking the prediction success limits proposed by Guest et al. [13] including 20% variability. Detailed information on all investigated DDI studies is provided in Section S4. AUClast: Area under the plasma concentration-time curve determined between first and last concentration measurements, C_{max}, maximum plasma concentration; DDI, drug–drug interaction.

which were generated without it. Thus, if more evidence were available showing that CYP2C9 induction can influence furmonertinib metabolism and this mechanism was incorporated into the model, the inaccuracy in higher dosage groups may be improved.

The first-ever developed PBPK model includes furmonertinib and its main active metabolite AST5902 and presents insights by investigating DDIs involving CYP3A4 perpetrators and auto-induction in long-term administration. In addition, the model was built and evaluated with a comprehensive clinical dataset covering wide

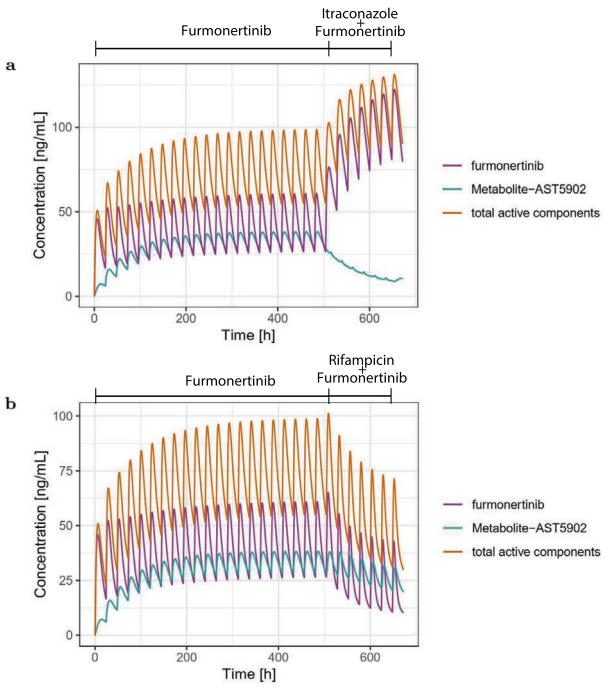

FIGURE 6 | Perspective simulations with the final furmonertinib model. Scenarios include 21 days of continuous dosing of 80 mg furmonertinib alone followed by 7 days of co-administration with CYP3A4 perpetrators (itraconazole (a); rifampicin (b)). CYP, cytochrome P450.

dosing ranges and two different populations. Incorporating the information gained from DDI studies, the model was used to predict furmonertinib exposure at steady state in the presence and absence of perpetrators, considering its properties as a substrate and an inducer. In the future, the model can be extended to further investigate DDIs between furmonertinib and other moderate or weak CYP3A4 perpetrators. Considering its auto-induction property, DDI scenarios between furmonertinib and CYP3A4 substrates (e.g., midazolam) can also be investigated. While we did not perform specific simulations of furmonertinib with additional agents in this study, our PBPK model is designed to accommodate such predictions. For example, if a patient were to require co-administration with an antidepressant such as fluvoxamine, a known CYP3A4 inhibitor, our model could simulate furmonertinib's plasma concentration profile under chronic co-administration with fluvoxamine or similar drugs with established PBPK parameters. This capability highlights the model's flexibility for future assessments of DDIs and its utility in optimizing dosing strategies for complex therapeutic regimens.

Author Contributions

Yali Wu, Helena Leonie Hanae Loer and Yifan Zhang analyzed the data. Yali Wu, Helena Leonie Hanae Loer, Uwe Fuhr and Thorsten Lehr performed the research. Yali Wu, Helena Leonie Hanae Loer, Uwe Fuhr and Thorsten Lehr wrote the manuscript. Yali Wu, Helena Leonie Hanae Loer, Yifan Zhang, Dafang Zhong, Yong Jiang, Jie Hu, Uwe Fuhr, Thorsten Lehr, and Xingxing Diao designed the research.

Conflicts of Interest

The authors declare no conflicts of interest.

References

1. J. G. Paez, P. A. Jänne, J. C. Lee, et al., "EGFR Mutations in Lung Cancer: Correlation With Clinical Response to Gefitinib Therapy," *Science* 304 (2004): 1497–1500.

2. S. V. Sharma, D. W. Bell, J. Settleman, and D. A. Haber, "Epidermal Growth Factor Receptor Mutations in Lung Cancer," *Nature Reviews Cancer* 7 (2007): 169–181.

3. L. V. Sequist, B. A. Waltman, D. Dias-Santagata, et al., "Genotypic and Histological Evolution of Lung Cancers Acquiring Resistance to EGFR Inhibitors," *Science Translational Medicine* 3 (2011): 75ra26.

4. National Medical Products Administration, "The State Food and Drug Administration has Conditionally Approved the Listing of Vometinib Mesylate Tablets" (2021), https://www.nmpa.gov.cn.

5. Y. Shi, S. Zhang, X. Hu, et al., "Safety, Clinical Activity, and Pharmacokinetics of Alflutinib (AST2818) in Patients With Advanced NSCLC With EGFR T790M Mutation," *Journal of Thoracic Oncology* 15 (2020): 1015–1026.

6. J. Meng, H. Zhang, J.-j. Bao, et al., "Metabolic Disposition of the EGFR Covalent Inhibitor Furmonertinib in Humans," *Acta Pharmacologica Sinica* 43 (2021): 494–503.

7. X.-y. Liu, Z. T. Guo, Z. D. Chen, et al., "Alflutinib (AST2818), Primarily Metabolized by CYP3A4, Is a Potent CYP3A4 Inducer," *Acta Pharmacologica Sinica* 41 (2020): 1366–1376.

8. Y. L. Wu, Y.-r. Xue, Z.-t. Guo, et al., "Furmonertinib (Alflutinib, AST2818) Is a Potential Positive Control Drug Comparable to Rifampin for Evaluation of CYP3A4 Induction in Sandwich-Cultured Primary Human Hepatocytes," *Acta Pharmacologica Sinica* 43 (2022): 747–756.

9. J. Heng, Q. Tang, X. Chen, et al., "Evaluation of the Pharmacokinetic Effects of Itraconazole on Alflutinib (AST2818): An Open-Label, Single-Center, Single-Sequence, Two-Period Randomized Study in Healthy Volunteers," *European Journal of Pharmaceutical Sciences* 162 (2021): 105815.

10. Y. T. Zhu, Y. F. Zhang, J. F. Jiang, et al., "Effects of Rifampicin on the Pharmacokinetics of Alflutinib, a Selective Third-Generation EGFR Kinase Inhibitor, and Its Metabolite AST5902 in Healthy Volunteers," *Investigational New Drugs* 39 (2021): 1011–1018.

11. H. L. H. Loer, C. Kovar, S. Rüdesheim, et al., "Physiologically Based Pharmacokinetic Modeling of Imatinib and N-Desmethyl Imatinib for Drug-Drug Interaction Predictions," *CPT: Pharmacometrics & Systems Pharmacology* 13 (2024): 926–940.

12. I. Hubatsch, E. G. Ragnarsson, and P. Artursson, "Determination of Drug Permeability and Prediction of Drug Absorption in Caco-2 Monolayers," *Nature Protocols* 2 (2007): 2111–2119.

13. X. Liu, W. Li, Y. Zhang, Y. Jiang, Q. Zhao, and D. Zhong, "Simultaneous Determination of Alflutinib and Its Active Metabolite in Human Plasma Using Liquid Chromatography–Tandem Mass Spectrometry," *Journal of Pharmaceutical and Biomedical Analysis* 176 (2019): 112735.

14. N. Hanke, S. Frechen, D. Moj, et al., "PBPK Models for CYP3A4 and P-gp DDI Prediction: A Modeling Network of Rifampicin, Itraconazole, Clarithromycin, Midazolam, Alfentanil, and Digoxin," *CPT: Pharmacometrics & Systems Pharmacology* 7 (2018): 647–659.

15. E. J. Guest, L. Aarons, J. B. Houston, A. Rostami-Hodjegan, and A. Galetin, "Critique of the Two-Fold Measure of Prediction Success for Ratios: Application for the Assessment of Drug-Drug Interactions," *Drug Metabolism and Disposition* 39 (2011): 170–173.

16. X. Liu, D. Feng, M. Zheng, Y. Cui, and D. Zhong, "Characterization of Covalent Binding of Tyrosine Kinase Inhibitors to Plasma Proteins," *Drug Metabolism and Pharmacokinetics* 35 (2020): 456–465.

17. Y. Wu, L. Chen, J. Chen, et al., "Covalent Binding Mechanism of Furmonertinib and Osimertinib With Human Serum Albumin," *Drug Metabolism and Disposition* 51 (2023): 8–16.

18. Y. Wu, L. Pan, Z. Chen, Y. Zheng, X. Diao, and D. Zhong, "Metabolite Identification in the Preclinical and Clinical Phase of Drug Development," *Current Drug Metabolism* 22 (2021): 838–857.

19. V. Pilla Reddy, M. Walker, P. Sharma, P. Ballard, and K. Vishwanathan, "Development, Verification, and Prediction of Osimertinib Drug-Drug Interactions Using PBPK Modeling Approach to Inform Drug Label," *CPT: Pharmacometrics & Systems Pharmacology* 7 (2018): 321–330.

20. H. J. Haiser and P. J. Turnbaugh, "Developing a Metagenomic View of Xenobiotic Metabolism," *Pharmacological Research* 69 (2013): 21–31.

21. S. M. Pond and T. N. Tozer, "First-Pass Elimination. Basic Concepts and Clinical Consequences," *Clinical Pharmacokinetics* 9 (1984): 1–25.

22. L. B. Bindels, A. M. Neyrinck, S. P. Claus, et al., "Synbiotic Approach Restores Intestinal Homeostasis and Prolongs Survival in Leukaemic Mice With Cachexia," *ISME Journal* 10 (2016): 1456–1470.

23. L. B. Bindels, A. M. Neyrinck, A. Loumaye, et al., "Increased Gut Permeability in Cancer Cachexia: Mechanisms and Clinical Relevance," *Oncotarget* 9 (2018): 18224–18238.

24. N. A. Helsby, W. Y. Lo, K. Sharples, et al., "CYP2C19 Pharmacogenetics in Advanced Cancer: Compromised Function Independent of Genotype," *British Journal of Cancer* 99 (2008): 1251–1255.

25. Z. Huang, M. J. Fasco, H. L. Figge, K. Keyomarsi, and L. S. Kaminsky, "Expression of Cytochromes P450 in Human Breast Tissue and Tumors," *Drug Metabolism and Disposition* 24 (1996): 899–905.

26. D. H. Josephs, D. S. Fisher, J. Spicer, and R. J. Flanagan, "Clinical Pharmacokinetics of Tyrosine Kinase Inhibitors: Implications for Therapeutic Drug Monitoring," *Therapeutic Drug Monitoring* 35 (2013): 562–587.

27. M. Michael and M. M. Doherty, "Tumoral Drug Metabolism: Overview and Its Implications for Cancer Therapy," *Journal of Clinical Oncology* 23 (2005): 205–229.

28. L. Rivory, K. Slaviero, and S. Clarke, "Hepatic Cytochrome P450 3A Drug Metabolism Is Reduced in Cancer Patients Who Have an Acute-Phase Response," *British Journal of Cancer* 87 (2002): 277–280.

29. Y. Chen, S. S. Ferguson, M. Negishi, and J. A. Goldstein, "Induction of Human CYP2C9 by Rifampicin, Hyperforin, and Phenobarbital Is Mediated by the Pregnane X Receptor," *Journal of Pharmacology and Experimental Therapeutics* 308 (2004): 495–501.

30. S. S. Ferguson, E. L. LeCluyse, M. Negishi, and J. A. Goldstein, "Regulation of Human CYP2C9 by the Constitutive Androstane Receptor: Discovery of a New Distal Binding Site," *Molecular Pharmacology* 62 (2002): 737–746.

31. J. M. Lehmann, D. D. McKee, M. A. Watson, T. M. Willson, J. T. Moore, and S. A. Kliewer, "The Human Orphan Nuclear Receptor PXR Is Activated by Compounds That Regulate CYP3A4 Gene Expression and Cause Drug Interactions," *Journal of Clinical Investigation* 102 (1998): 1016–1023.

32. G. Bertilsson, J. Heidrich, K. Svensson, et al., "Identification of a Human Nuclear Receptor Defines a New Signaling Pathway for CYP 3 A Induction," *Proceedings of the National Academy of Sciences of the United States of America* 95 (1998): 12208–12213.

33. B. Blumberg, W. Sabbagh, Jr., H. Juguilon, et al., "SXR, a Novel Steroid and Xenobioticsensing Nuclear Receptor," *Genes & Development* 12 (1998): 3195–3205.

34. T. Sueyoshi, T. Kawamoto, I. Zelko, P. Honkakoski, and M. Negishi, "The Repressed Nuclear Receptor CAR Responds to Phenobarbital in Activating the Human CYP2B6 Gene," *Journal of Biological Chemistry* 274 (1999): 6043–6046.

Supporting Information

Additional supporting information can be found online in the Supporting Information section.